JOURNAL OF SYNCHROTRON RADIATION

ISSN 1600-5775

Received 9 October 2018
Accepted 28 April 2019

Edited by T. Tschentscher, European XFEL, Germany

[1] This article will form part of a virtual special issue on X-ray free-electron lasers.

Keywords: free-electron laser; hard X-rays; bunch compression; coherent synchrotron radiation; stability; arrival timing jitter.

FEL performance achieved at PAL-XFEL using a three-chicane bunch compression scheme[1]

Heung-Sik Kang,* Haeryong Yang, Gyujin Kim, Hoon Heo, Inhyuk Nam, Chang-Ki Min, Changbum Kim, Soung Youl Baek, Hyo-Jin Choi, Geonyeong Mun, Byoung Ryul Park, Young Jin Suh, Dong Cheol Shin, Jinyul Hu, Juho Hong, Seonghoon Jung, Sang-Hee Kim, KwangHoon Kim, Donghyun Na, Soung Soo Park, Yong Jung Park, Jang-Hui Han, Young Gyu Jung, Seong Hun Jeong, Min Jae Kim, Hong Gi Lee, Sangbong Lee, Woul-Woo Lee, Bonggi Oh, Hyung Suck Suh, Ki-Hyeon Park, Heung-Soo Lee, D. Z. Khan, T. O. Raubenheimer and Juhao Wu

Pohang Accelerator Laboratory, 80 Jigokro-127-beongil, Nam-gu, Pohang, Kyungbuk 37673, South Korea. *Correspondence e-mail: hskang@postech.ac.kr

PAL-XFEL utilizes a three-chicane bunch compression (3-BC) scheme (the very first of its kind in operation) for free-electron laser (FEL) operation. The addition of a third bunch compressor allows for more effective mitigation of coherent synchrotron radiation during bunch compression and an increased flexibility of system configuration. Start-to-end simulations of the effects of radiofrequency jitter on the electron beam performance show that using the 3-BC scheme leads to better performance compared with the two-chicane bunch compression scheme. Together with the high performance of the linac radiofrequency system, it enables reliable operation of PAL-XFEL with unprecedented stability in terms of arrival timing, pointing and intensity; an arrival timing jitter of better than 15 fs, a transverse position jitter of smaller than 10% of the photon beam size, and an FEL intensity jitter of smaller than 5% are consistently achieved.

1. Introduction

PAL-XFEL is Korea's first, and the world's third, hard X-ray free-electron laser facility, following the Linac Coherent Light Source (LCLS) (Emma *et al.*, 2010) in the USA and the SPring-8 Angstrom Compact Free Electron Laser (SACLA) (Ishikawa *et al.*, 2012) in Japan. After the successful commissioning of PAL-XFEL in 2016, its user service operation began in June 2017 (Kang *et al.*, 2017). Hard X-ray free-electron lasers (XFELs), including the European XFEL (Weise & Decking, 2017) and SwissFEL (Milne *et al.*, 2017), have successfully provided users with high-spectral intensity photon beams, proving to be invaluable tools in the research and development of many disciplines across all science.

Electron beam based alignment incorporating undulator radiation spectrum analysis is fully utilized for better performance of hard XFELs (Kang *et al.*, 2017). The electron beam itself, which undergoes the process of acceleration and compression to ultra-relativistic energies (~10 GeV) and durations of tens of femtoseconds (~50 fs at FWHM), contributes to the FEL performance as well. During transport to the undulators, the electron beam experiences a myriad of effects that could potentially spoil its quality and consequently degrade the FEL performance. The longitudinal space charge (LSC), coherent synchrotron radiation (CSR) and micro-bunching instability (MBI) are among the most predominant

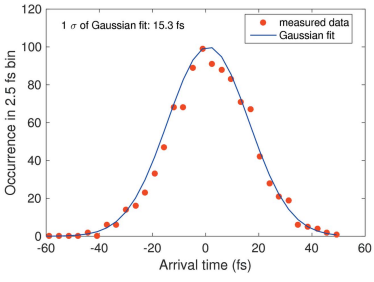

phenomena that a beam encounters during transport. These effects have motivated many studies in efforts to minimize them and improve the FEL machine performance (Venturini *et al.*, 2015; Saldin *et al.*, 2002, 2004; Heifets *et al.*, 2002; Huang & Kim, 2002).

One of the main causes of poor FEL performance is the emittance dilution induced by CSR in bunch compressors. Hard XFELs require a beam current of over 2 kA to lower the gain length and increase the FEL intensity. However, increasing the beam current through magnetic bunch compression can lead to bend-plane emittance growth and energy spread because of CSR in the dipoles of the compressor. The larger the bend angle of the bunch compressor, the more the emittance growth. Also, beam acceleration configurations with radiofrequency (RF) phases closer to the crest are the least sensitive to RF amplitude and phase errors (Borland, 2001*a*), which contribute to the jitter performance of the electron beam. Therefore, the bend angle of the dipoles in a bunch compressor is preferred to be small to reduce emittance growth caused by CSR, and beam acceleration with RF phases closer to the crest is preferred to reduce energy jitter of the electron beam. However, a smaller bend angle to reduce emittance growth entails a larger linear energy chirp, h, at the preceding RF sections, meaning the RF phase moves farther away from the crest; having RF phases closer to the crest for the reduced energy jitter entails a larger R_{56}, meaning a larger bend angle of the bunch compressor. Having both small h and small R_{56} is incompatible in this sense.

To realize both a small R_{56} at the last bunch compressor to reduce emittance growth caused by CSR and a small energy chirp to reduce energy jitter at the end of the linac, a three-chicane bunch compression (3-BC) scheme was adopted for PAL-XFEL (see Fig. 1). It is feasible because the overall R_{56} of the 3-BC scheme can be made larger than the two-chicane bunch compression (2-BC) scheme so that the required energy chirp can be reduced. This scheme allows both beam acceleration with RF phases closer to the crest and a smaller bend angle at the last bunch compressor (Kang *et al.*, 2011, 2012*a*). The addition of the third bunch compressor also allows an increased flexibility of the system configuration with respect to the compression factor and energy chirp among the compressors. MBI is expected to be more pronounced in the 3-BC scheme than the 2-BC because the additional stages of bunch compression may introduce a greater MBI gain.

PAL-XFEL consists of a 10 GeV S-band normal conducting linac and two undulator lines: a hard X-ray undulator line (HX1) and a soft X-ray undulator line (SX1) (see Fig. 1). The hard XFEL line contains five acceleration sections, three magnetic bunch compressor chicanes (BC1, BC2 and BC3H), an achromatic dogleg transport line with a bend angle of 0.5° and the hard X-ray line undulators (HX1). In Fig. 1, L0 represents the 135 MeV injector, consisting of a photocathode RF gun and two S-band accelerating structures. A laser heater system to reduce MBI is placed immediately after the injector (Lee *et al.*, 2017). A 75 cm-long X-band cavity is located immediately after L1 for linearization. The soft XFEL line, which branches out from the end of L3A, at which point the beam energy is 3 GeV, consists of two double-bend achromats whose dipole bend angles are 3°, one RF station (L3S), the third magnetic bunch compressor chicane (BC3S), and the soft X-ray line undulators (SX1). The third bunch compressor for each beamline (BC3H for HX and BC3S for SX) is placed after the switch yard of the 3 GeV point of the linac. The peak current after the second bunch compressor is designed to be below 1 kA to minimize CSR kicks along the 3° achromatic beam transfer line to the soft X-ray line undulators. Twenty undulator segments are installed in HX1, and seven segments are installed in SX1. We adopted the European XFEL undulator design (Pflueger *et al.*, 2013), which features a 5 m-long, planar, permanent magnet, and an out-vacuum variable-gap undulator, and modified its magnet design according to the PAL-XFEL undulator parameters. Designed and measured parameters of PAL-XFEL are listed in Table 1.

Even though the 3-BC scheme operation is the baseline for PAL-XFEL, three configurations of bunch compressors are available for operation, as shown in Table 2: 3-BC operation (BC1-BC2-BC3) and 2-BC operations (BC1-BC2 and BC1-BC3). The RF phase and bunch compressor parameters of the 3-BC configuration (BC1-BC2-BC3) are the parameters currently used in normal operation.

The manuscript is organized as follows. In Section 2, we discuss the analytical estimation of the CSR kick for the three configurations of bunch compressors. In Section 3, we discuss the results of start-to-end simulations to compare the three

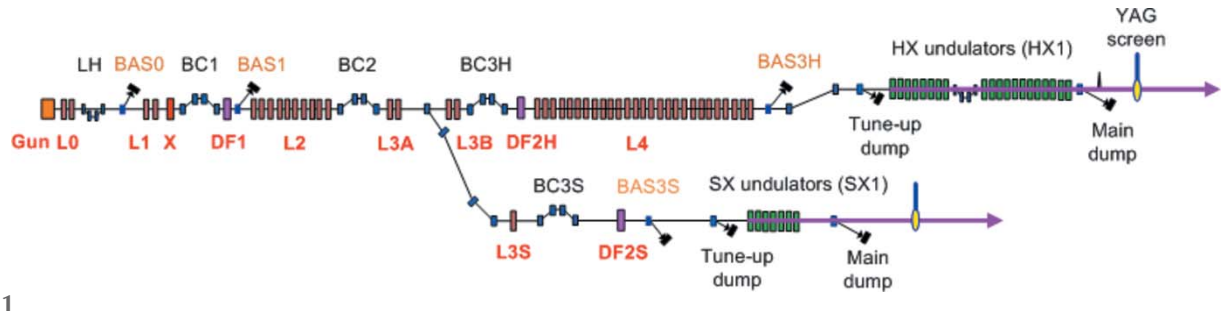

Figure 1
Schematic diagram of PAL-XFEL. L0: injector; L1, L2, L3A, L3B, L4 and L3S: acceleration sections; X: X-band linearizer cavity; DF1, DF2H and DF2S: deflector cavities; LH: laser heater; BC1, BC2, BC3H and BC3S: magnetic bunch compressor chicanes, whose dipoles are rectangles in blue; BAS0, BAS1, BAS3H and BAS3S: beam analysis stations, each of which consists of a dipole (rectangle in blue), a YAG screen and a dump (rectangle in black).

Table 1
Designed and measured parameters of PAL-XFEL.

	Designed	Measured
Electron beam		
Electron energy (GeV)	10	9.47
Slice emittance (mm mrad)	0.5	0.4
Beam charge (nC)	0.2	0.18
Peak current at undulator (kA)	3.0	3.5
Pulse repetition rate (Hz)	60	60
Undulator (HX1)		
Undulator period (m)	0.026	
Undulator parameter, K	1.5–1.9	
Undulator length (m)	5.0	
Number of undulators	20	
Photon beam		
FEL radiation wavelength (nm)	0.1	0.1
Photons per pulse (10^{11})	2.6	7.0

configurations in terms of the RF jitter effects on the electron beam properties. In Section 4, we discuss the electron beam performances achieved from the 3-BC scheme operation with the measured data of projected emittance, relative mean energy jitter, arrival time jitter, transverse orbit jitter, and laser heater impact on FEL performance. Finally, in Section 5, we discuss the FEL performance in terms of FEL intensity, central wavelength jitter and pointing jitter.

2. Analytical estimation of the CSR kick for the three configurations of bunch compressors

In a chicane-type bunch compressor, the mean energy offset and the standard deviation of the energy offset with $\delta = (p - p_o)/p_o$, where p_o is the central momentum, are as follows (Borland, 2001*b*),

$$\langle\delta\rangle = -0.3505\,\frac{r_e Q L_b}{e\gamma(R^2\sigma_s^4)^{1/3}}, \tag{1}$$

$$\delta_{rms} = 0.2459\,\frac{r_e Q L_b}{e\gamma(R^2\sigma_s^4)^{1/3}}, \tag{2}$$

where L_b is the length of the dipole, e is the electron charge, γ is the relativistic factor of the electron beam, R is the bend radius of the dipole, Q is the bunch charge, and σ_s is the r.m.s. bunch length. The r.m.s. geometric emittance, ε, increases by a factor $(1 + \theta^2\langle x^2\rangle\langle\Delta\delta^2\rangle/\varepsilon^2)^{1/2}$, where θ is the dipole bend angle, which is minimized by minimizing the r.m.s. beam size at the exit of the last dipole of the chicane (Borland, 2001*a*). The adoption of optics with smaller betafunction, β_x, in the second half of the bunch compressor, as well as a smaller bend angle in the bunch compressor, can diminish the emittance growth caused by CSR.

The CSR-induced perturbation kick is $\Delta x' = \eta'\sigma_{\delta,CSR}$, where $\sigma_{\delta,CSR}$ is $\langle\delta\rangle$ of equation (1), given at the end of the last dipole magnet of a bunch compressor, where, for a small bend angle ($\theta \ll 1$), $\eta' \simeq \theta$. The CSR-induced perturbation kicks for the three configurations of bunch compressors, which are calculated with the parameters of the last bunch compressor, are listed in Table 2. It is clear that the 3-BC configuration is superior to BC1-BC2 and BC1-BC3 in terms of the CSR-induced kick. The BC1-BC3 configuration takes advantage of the fact that BC3 can perform the final compression at a much higher energy than that of BC2, thereby reducing the impact that the CSR will have on the induced energy spread via its γ^{-1} behavior in equations (1) and (2).

Table 2
Three configurations of bunch compressors for start-to-end simulation.

	BC1-BC2-BC3	BC1-BC2	BC1-BC3
RF phases (°)			
L1	−11.6	−16.6	−16.6
X	−178.0	−178.0	−178.0
L2	−21.95	−32.38	−39.5
L3	−8.0	0.0	−39.5
L4	1.0	1.0	1.0
BC1			
θ (°)	4.97	4.97	4.97
R_{56} (mm)	−66.7	−66.7	−66.7
BC2			
θ (°)	3.0	2.5	0.0
R_{56} (mm)	−36.7	−26.9	
BC3			
θ (°)	1.6	0	2.2
R_{56} (mm)	−11.6		−22.0
Peak current (kA)	2.94	2.97	2.94
CSR-induced kick, $\Delta x'$	2.65×10^{-6}	7.63×10^{-6}	4.50×10^{-6}

Cancelation of CSR kicks can be achieved by setting the phase advance π between the bunch compressors such that the kicks cancel each other out (Douglas, 1998; Mitri *et al.*, 2013; Hajima, 2003). The idea of the π-phase advance CSR cancelation is not implemented in the current 3-BC scheme operation of PAL-XFEL. In the current design, the betatron phase advances from the end of BC1 to the end of BC2 and from the end of BC2 to the end of BC3 are 1.706 and 0.773, respectively, away from the π-phase advance (the phase advance is described as $2\pi\nu$, and a π-phase difference corresponds to 0.5 of ν). The 3-BC scheme enables the dipole bend angle of the chicane to be relatively small, which results in reduction of the CSR kick amplitude to a level not necessary to use the π-phase advance CSR cancelation. In the actual accelerator operation, it is not practical to maintain the fixed phase advance between bunch compressors.

3. RF jitter effect simulation for the three configurations of bunch compressors

The CSR-induced perturbation kicks listed in Table 2 are simple estimations based on equation (1) using only the parameters of beam energy (3.6 GeV for the 3-BC and BC1-BC3, and 2.5 GeV for BC1-BC2), peak current (3 kA) and dipole magnet at the last bunch compressor. It does not take into consideration the variations of actual electron beam properties during the bunch compression, which depend on the configuration of bunch compressors. In the process of acceleration and compression, the electron beam properties

are quite variable because they are subject to errors like the RF amplitude and phase jitters. Each electron bunch must see a different amplitude and phase of the RF field at each RF station because of the RF system jitters, so that all the beam parameters, such as peak current and energy, and thus CSR kick amplitude, are different from pulse to pulse.

Start-to-end simulation using the *Elegant* code (Borland, 2000) was carried out to evaluate the RF jitter effect on the electron beam properties. We compared the electron beam performances in terms of projected emittance, relative energy jitter and arrival time jitter for the three configurations of bunch compressors of the PAL-XFEL linac. For this comparison, the parameters of the three configurations are chosen to have the peak current after the last bunch compressor to be around 3 kA and the correlated energy spread at the end of linac smaller than the FEL parameter (see Table 2).

Fig. 2 shows the actual stability of the RF system (phase and amplitude jitters in r.m.s.) measured in December 2017 and in April 2018. The RF system performance was improved in the beginning of 2018 by changing the focusing magnet power supplies of the S-band klystrons from the 1000 p.p.m. stability class to the 100 p.p.m. for the L0, L1 and L2 sections. The phase and amplitude jitters of the L1 section were improved to better than 0.015° and 0.01%, and better than 0.03° and 0.015% in the L2 section. However, the stability of the X-band linearizer RF system was still poor, 0.07° in phase and 0.15% in amplitude, even though it was improved from 0.12° in phase and 0.23% in amplitude of the December 2017 data.

For the jitter study, we used four different cases of RF stability (phase and amplitude jitters in r.m.s.) of the 47 RF stations in the hard X-ray line. The jitter of April 2018 of Fig. 2 was used as the RF jitter case RJ-1, RJ-2 is the jitter of December 2017, RJ-3 (not depicted in Fig. 2) was selected to have the phase jitter of 0.05° and amplitude jitter of 0.02% in L1 and L2, and the phase jitter of 0.1° and amplitude jitter of 0.05% in L3 and L4 (assumed as the bad jitter case, on average two times higher than RJ-2), and RJ-4 was selected to have the phase jitter of 0.1° and amplitude jitter of 0.05% in L1, L2, L3 and L4 as the worst case. In this simulation, other errors such as the incoming timing jitter from the injector and the jitters of magnet power supplies are not included; thus, the jitter estimated from the simulation would be an underestimation of the actual jitter performance of the linac.

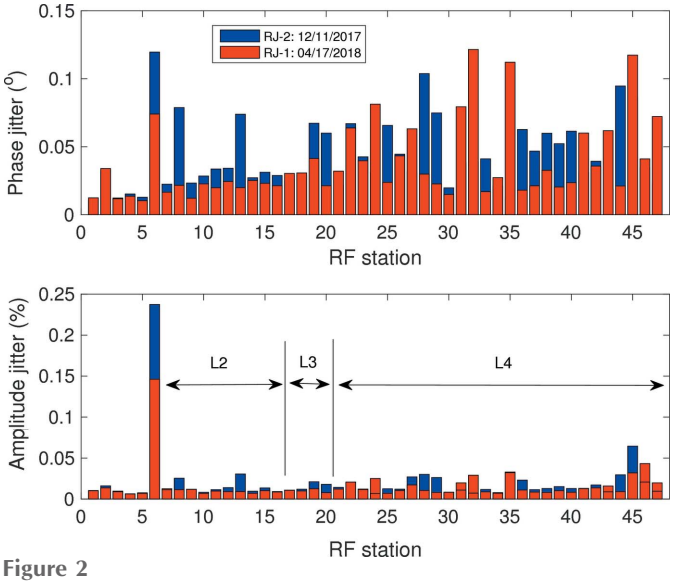

Figure 2
RF stability of 47 RF stations, phase jitter (upper figure) and amplitude jitter (lower figure) measured in December 2017 and April 2018. RF station No. 1 is the gun, Nos. 2 to 3 belong to the injector (L0), Nos. 4 to 5 belongs to the L1 section, No. 6 is an X-band linearizer, Nos. 7 to 16 belong to the L2 section. The jitter measured in April 2018 was used as the RF jitter case RJ-1 and the jitter measured in December 2017 was used as RJ-2 for the RF jitter effect simulation.

Fig. 3 shows the electron beam jitter performance at the entrance of the undulator line (HX1), calculated for the three configurations of bunch compressors (BC1-BC2, BC1-BC3 and 3-BC) with the four different RF jitter cases of Fig. 2. Both the relative energy jitter and arrival time jitter are the r.m.s. values of their corresponding outputs from the 300 *Elegant* runs. The projected emittance (ε_x) is the mean value with error-bar from the 300 *Elegant* outputs.

The simulation result in Fig. 3(*a*) shows that the projected emittances (ε_x) of the 2-BC configurations (BC1-BC2 and BC1-BC3) are significantly larger than that of the 3-BC as expected from the analytical estimations of the CSR kick in Table 2, and the error bar increases significantly as the RF jitter increases in all three configurations. The error bar is most dominant in the BC1-BC2 configuration because the RF jitter changes beam properties significantly such that CSR is stronger or weaker. The vertical emittances of the three configurations are the same as 4.7×10^{-7} mm mrad and not affected by the RF jitters.

Both the relative energy jitter and arrival time jitter increase significantly as the RF jitter increases as shown in Figs. 3(*b*) and 3(*c*). The relative energy jitter performance is worst in the BC1-BC3 configuration and similar in both the 3-BC and the BC1-BC2 configuration. The arrival time jitter performance is worst in the BC1-BC2 configuration and similar in both the 3-BC and the BC1-BC3 configuration. Under the current condition of RF system jitter of RJ-1, the 3-BC configuration shows the best performance in terms of projected emittance, relative mean energy jitter and arrival time jitter, indicating the 3-BC can provide the best FEL performance among the three.

4. Electron beam performance achieved from the 3-BC scheme operation

PAL-XFEL uses the 3-BC scheme as the nominal operation mode. As discussed in the previous section, the 3-BC scheme is less vulnerable to RF jitters. This scheme enables the delivery of a very stable electron beam to the undulators, which subsequently generates a very stable FEL beam.

The RF and bunch compressor parameters of the 3-BC scheme operation currently in use, listed in Table 2, have been optimized since June 2017 when the FEL commissioning was completed with the 2-BC scheme (BC1-BC2). The 2-BC scheme had been used for one year, in 2016, for the FEL

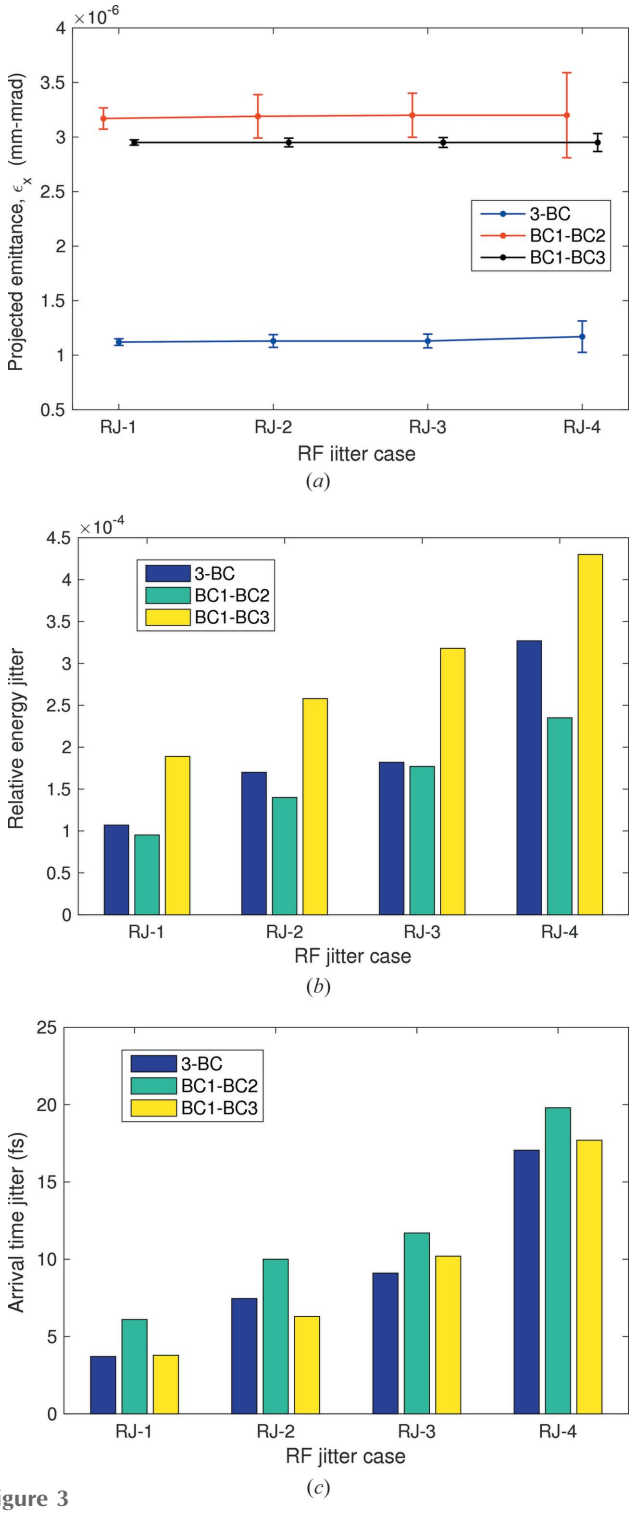

Figure 3
Electron beam jitter performance obtained from the *Elegant* simulation for the three configurations of bunch compressors (BC1-BC2, BC1-BC3 and 3-BC) and the four different RF jitter cases of Fig. 2: (*a*) projected emittance (ε_x), (*b*) relative mean energy jitter, and (*c*) arrival time jitter. Both the relative mean energy jitter and arrival time jitter are the r.m.s. values of their corresponding outputs from the 300 *Elegant* runs. The projected emittance (ε_x) is the mean value with error bar from the 300 *Elegant* outputs. In the simulation, other errors such as the incoming timing jitter from the injector and the jitters of magnet power supplies are not included; thus, the jitters, particularly the arrival time jitter, estimated from the simulation would be an underestimation of the actual jitter performance of the linac.

commissioning because this scheme was simple to set up. The compression ratios of the 3-BC scheme are 2.0/4.8/13.0. The compression ratio of BC1 is quite small, which helps to reduce the CSR kick at a relatively low beam energy of 350 MeV at BC1, while the compression ratio of BC3 is relatively high, but the CSR kick is not serious because the beam energy is relatively high, 3.6 GeV. The bunch length measured with a deflector at the exit of BC3 is 6.18 ± 0.46 µm, and with this and the beam charge of 180 pC the peak current is calculated to be 3.5 kA.

4.1. Projected emittance

There are five locations of the emittance measurement in the hard X-ray FEL line: three locations using a quad scan with a YAG screen [at the end of L0 (injector), at the entrance of the X-linearizer, and at the entrance of L2], and two locations using five wire scanners, at the end of L4 and the undulator line. There are four to five matching quads upstream of each emittance measurement location (except at the end of L0, where there is no matching quad).

The lattice of the hard X-ray undulator line (Kang *et al.*, 2014) is 15 periods of FODO lattice with drift space that can potentially accommodate 30 undulators, although only 20 undulators are currently in place situated between the quads. The betatron phase advance of the lattice is 40° per cell. Five wire scanners (Kim *et al.*, 2016, 2018) are placed at the center of the drifts of the undulator line FODO lattice. The locations of the wire scanners were selected among drift spaces, where undulators are not placed, aiming to have an accumulated betatron phase advance of greater than 120° between the first wire scanner and the last: three wire-scanners are placed upstream of the first undulator, one wire scanner is located at the self-seeding section in the middle of the undulator line, and one wire scanner is placed immediately after the last undulator, such as at 0, 40, 80, 160 and 260°, respectively. The wire material is a 34 µm-thick carbon wire. It takes 2 min to finish one plane emittance measurement using five wire scanners, so it takes only 4 min for both horizontal and vertical planes. The five-wire-scanner measurement gives us the beam profiles at five different places of the undulator line, the projected emittance, and the Twiss parameters at the matching point. By adjusting the five quadrupoles located upstream of the FODO lattice, the measured Twiss parameters can be matched to the design lattice. This kind of arrangement of wire-scanners enables us to measure the exact size of the e-beam interacting with the photon beam along the undulator line.

The injector section, consisting of a photocathode RF gun (Chae *et al.*, 2011) and two S-band accelerating structures, generates a low-emittance beam with a projected emittance of 0.34 mm mrad (horizontal) and 0.33 mm mrad (vertical) at an energy of 135 MeV and a beam charge of 150 pC. To remove the horn shapes from the compressed bunch current profile (Zhou *et al.*, 2015; Ding *et al.*, 2016), an energy collimator was used at the first bunch compressor (BC1). This helps to increase the FEL intensity, so that the injector beam charge

was increased to 240 pC; then, the beam charge at BC1 was reduced to 180 pC by the collimator. Accordingly, the projected emittance of the injector increased to 0.45 ± 0.02 mm mrad (horizontal) and 0.43 ± 0.01 mm mrad (vertical) as a result of the higher bunch charge.

Fig. 4 shows the beam sizes along the undulator line, emittances and Twiss parameters of the horizontal and vertical planes measured with the wire scanners in the undulator line. The measured emittances ($\gamma\varepsilon$) at the undulator line are 0.72 ± 0.03 mm mrad (horizontal) and 0.58 ± 0.03 mm mrad (vertical). The right-hand figures in Figs. 4(*a*) and Fig. 4(*b*) represent a phase space normalized to a 1 mm mrad emittance beam, depicted by the green circle. The mismatch parameter in the figure, $\xi = (1/2)(\hat{\beta}\gamma - 2\alpha\hat{\alpha} + \beta\hat{\gamma})$, is defined as the difference between the measured Twiss parameters and the design lattice Twiss parameters, where α, β and γ are the design Twiss parameters and $\hat{\alpha}$, $\hat{\beta}$ and $\hat{\gamma}$ are the measured Twiss parameters. The perfect matching case of $\alpha = \hat{\alpha}$, $\beta = \hat{\beta}$ and $\gamma = \hat{\gamma}$ corresponds to $\xi = 1$. The mismatch parameter (ξ) in the figure is as small as 1.01 (horizontal) and 1.02 (vertical), close to the perfect matching, and the beam sizes of both planes are almost uniform along the undulator line. Optimizing the matching of the electron beam along the 100 m-long undulator line facilitates maximizing the spatial overlap between the e-beam and photon beam.

Fig. 5 shows the horizontal beam profiles measured at two different wire scanner locations (WS3 and WS5) of the undulator line before and after the Twiss parameter matching. The distance marked in the figure represents the peak position shift of the electron beam distribution after the matching, while the position of the center of mass appears unchanged through the matching. After the matching, the electron beam distribution recovered from an asymmetrical to a Gaussian distribution.

The measured emittances from the injector to the undulator line are listed in Table 3. The quad scan emittance measurement using a YAG screen is reliable only for the injector and the X-linearizer, while others (at the entrance of L2), not listed in the table, give a high value of emittance, higher than 1.5 mm mrad, with a large error. The vertical emittance at the entrance of the X-linearizer is 0.54 ± 0.02 mm mrad, similar to

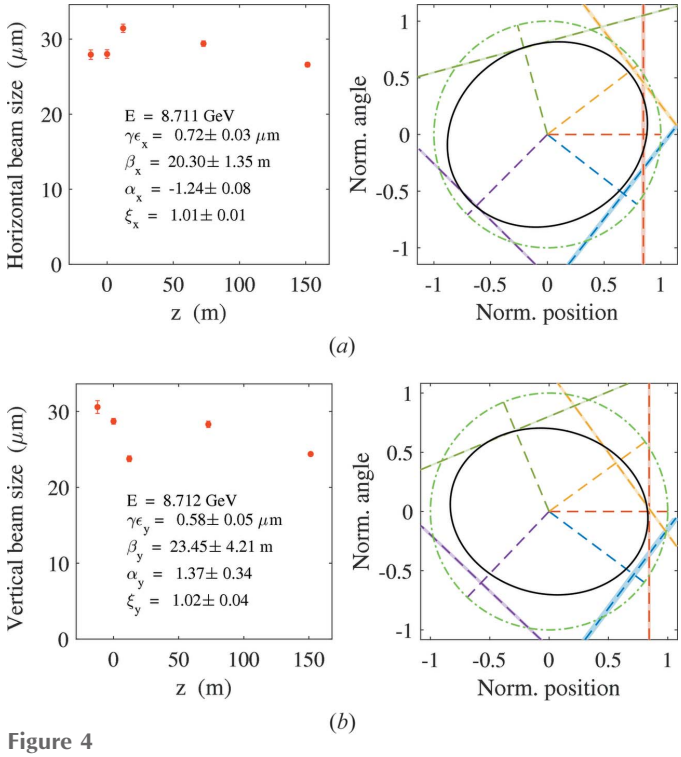

Figure 4
Measurement of beam sizes and emittances using wire scanners in the undulator FODO lattice. Beam sizes along the undulator line and normalized phase space of the horizontal plane (*a*) and the vertical plane (*b*). The horizontal axis of the beam size figures [left-hand figure in (*a*) and (*b*)] represents the distance along the undulator line and the second wire-scanner is located at $z = 0$. $\gamma\varepsilon$, β, α in the left-hand figures of (*a*) and (*b*) are the measured Twiss parameters at $z = 0$. The green circle in the phase space diagrams [right-hand figures in (*a*) an (*b*)] represents a phase space of a 1 mm mrad emittance beam. The five colored lines of the phase space diagram represent the position and angle of the measurement for the five wire scanners and those inside the circle represent betatron phase advance.

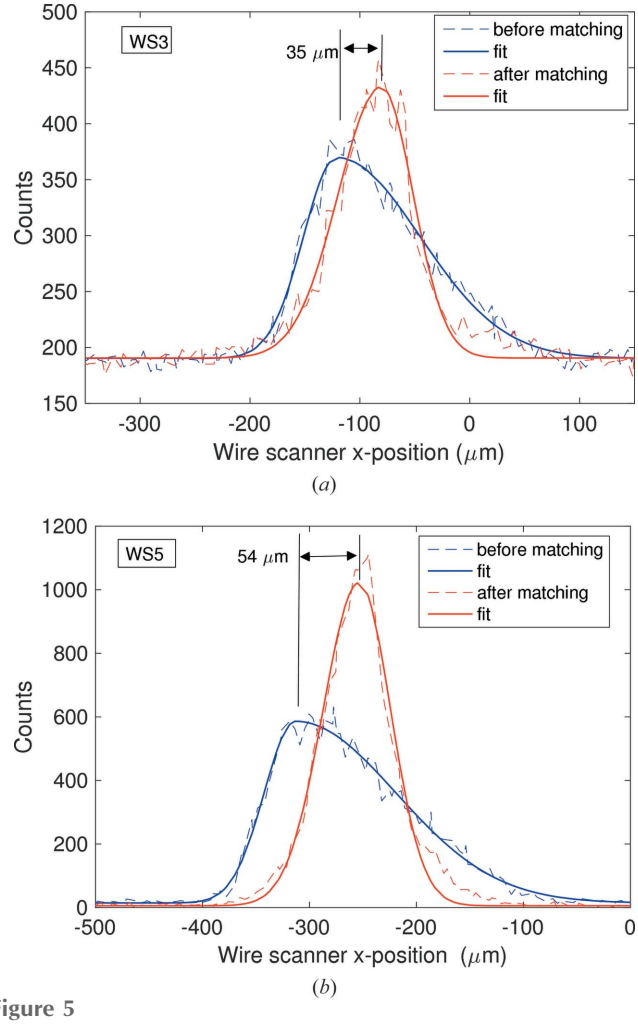

Figure 5
Horizontal e-beam profiles measured at WS3 (*a*), the third scanner in Fig. 4, and WS5 (*b*), the fifth scanner, before and after the lattice matching. The distance marked in the figure represents the peak position shift of the electron beam distribution after the matching, while the position of center of mass appears unchanged after the matching.

Table 3
Measured projected emittances from the injector to the undulator line.

Location of measurement	Measurement method	Horizontal emittance (mm mrad)	Vertical emittance (mm mrad)
Injector	Quad scan with YAG	0.45 ± 0.02	0.43 ± 0.01
X-linearizer	Quad scan with YAG	0.44 ± 0.02	0.54 ± 0.02
End of L4	Five wire scanners	0.68 ± 0.02	0.56 ± 0.03
Undulator line	Five wire scanners	0.72 ± 0.03	0.58 ± 0.03

the undulator line. The horizontal emittance was increased from 0.45 μm at the injector to 0.72 μm at the undulator line. The horizontal and vertical emittances measured at the undulators are 0.72 μm and 0.58 μm, respectively, while those of the *Elegant* simulation results are 1.12 μm and 0.47 μm, respectively. The fact that the horizontal emittance of the simulation is much bigger than the measurement is because in the simulation the horn shapes from the compressed bunch current profile is not properly removed by an energy collimator at BC1.

The CSR-induced tilt along the bunch in the horizontal plane was corrected using the tweak quads at the chicanes, and the vertical plane tilt along the bunch was also minimized by placing the e-beam on the axis of the X-band linearizer, which exerts a strong time-dependent RF kick on the beam. After the beam tilt along the bunch was minimized, the Twiss parameters obtained from the projected emittance measurements were valid for both the center and along the bunch (Kang *et al.*, 2019), which enables a proper setting of matching quads to be found for matching the measured Twiss parameters to the design. Using this emittance measurement and lattice matching, we could maintain the projected emittance at less than 0.72 mm mrad (horizontal) and 0.58 mm mrad (vertical) from the injector to the undulators.

4.2. Relative mean energy jitter

The e-beam energy jitter performance strongly depends on the RF system jitter performance, as shown in Fig. 3(*b*). Fig. 6 shows the relative e-beam mean energy jitter measured at four dispersive locations in December 2017 and in April 2018, which accounts for the effect of RF jitter improvement of Fig. 2. The energy jitter at BC2 was improved by a factor of two, which was attributed to the stability improvement of both the L2 and X-band RF system, as shown in Fig. 2. The e-beam mean energy jitter at the dump was also improved from 0.019% of December 2017 to 0.013% of April 2018.

4.3. Arrival time jitter

The arrival time of the electron beam was measured with a 2.826 GHz phase cavity located at the end of the hard X-ray undulator line (HX1), just prior to the main dump dipole (Shin *et al.*, 2018). The phase cavity has two output pickups (BAM1 and BAM2), whose detected RF signals are processed using the same electronics to evaluate the systematic error of the measurement system. The arrival time measured before December 2017 was 18.8 fs r.m.s., and the deconvoluted jitter

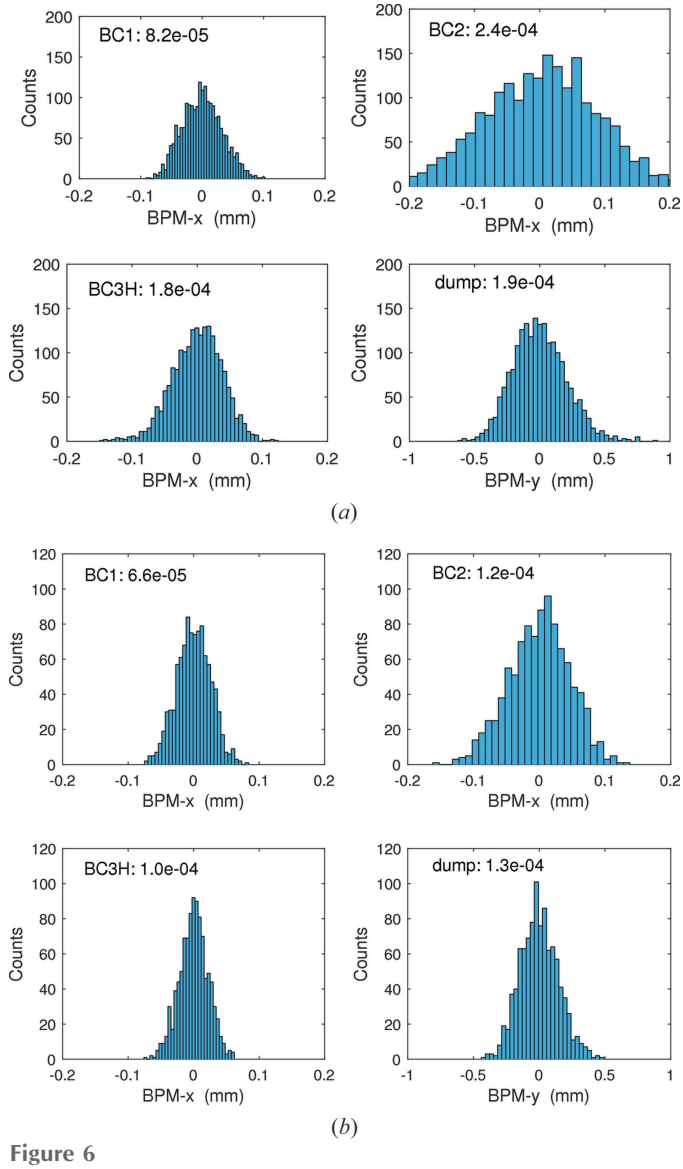

Figure 6
Relative e-beam mean energy jitter measured at four dispersive locations in December 2017 (*a*) and April 2018 (*b*): the BPMs at the center of the bunch compressors (BC1, BC2 and BC3H) and the BPM at the main dump.

of the electron bunch arrival time is 15.1 fs. The arrival time jitter measured in April 2018 was improved to 15.3 fs, as shown in Fig. 7. Deconvoluting the systematic error of 9.4 fs in Fig. 7(*b*), the actual arrival time jitter is as small as 12.1 fs r.m.s.

4.4. Transverse orbit jitter

As discussed in Section 3, the amplitude and phase jitters of the RF system introduce a different amplitude of the CSR-induced transverse kick, $\Delta x'$, for each pulse bunch. This kind of transverse kick induces betatron oscillation of the orbit along the downstream of the source point and down to the undulator line. A large variation of orbit along the undulator line may degrade the overlap between the e-beam and FEL beam. The pulse-by-pulse orbit jitter lasts only while the source of the transverse kick exists and is as fast as the elec-

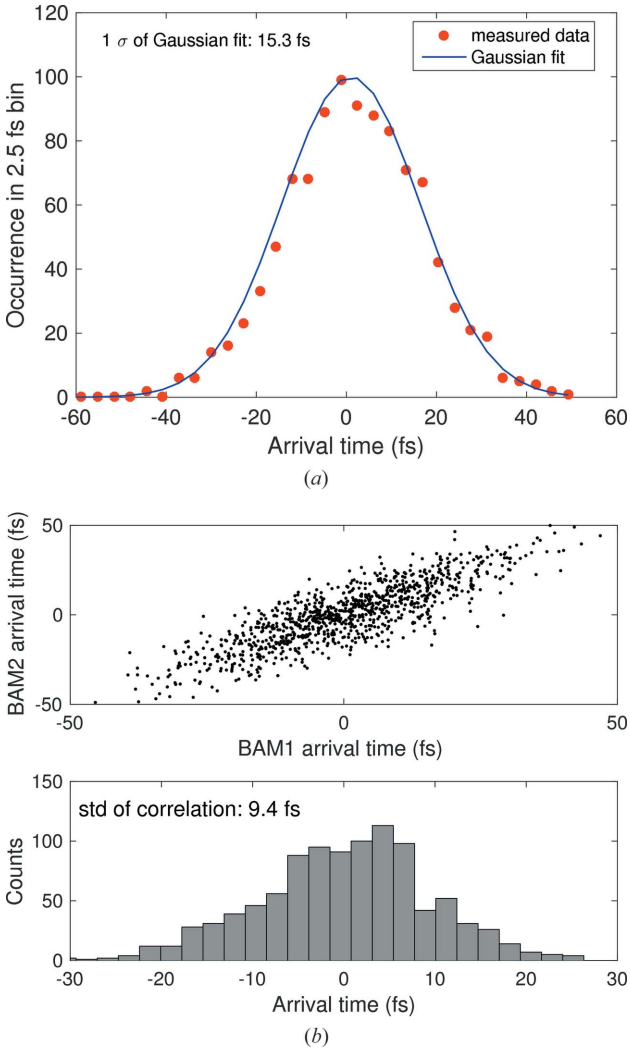

Figure 7
(*a*) Histogram of electron bunch arrival times measured with a 2.826 GHz phase cavity at the end of the HX undulator line HX1 with data being sampled for 3.3 min. (*b*) Correlation plot of BAM1 and BAM2. In (*a*), the Gaussian fit of electron bunch arrival time jitter is 15.3 fs in r.m.s.

tron beam pulse length, so that it is not possible to correct the orbit jitter of its own. Minimizing the transverse kick amplitude is the only way to minimize the orbit jitter. Nevertheless, to correct a slow change in orbit due to ground motion and others, we use an orbit feedback covering from the injector end to the end of the undulator line with a correction speed of 1 Hz for the 30 Hz beam rate.

To observe a pulse-by-pulse orbit jitter caused by a very fast transient kick, 1000 shots of the orbit from the injector to the main dump for the horizontal and vertical planes were measured (see Fig. 8). The slow orbit feedback was turned off for this measurement (for 33 s at the 30 Hz beam rate). The r.m.s. of the orbit variation along the undulator line (from BPM-112 to BPM-133) is smaller than 4.2 μm in the horizontal plane and 2.5 μm in the vertical plane, which are in the range of 10% of the e-beam size, as shown in Fig. 4. The pulse-by-pulse orbit jitter caused by the fast-transient kick is not serious in the 3-BC scheme operation.

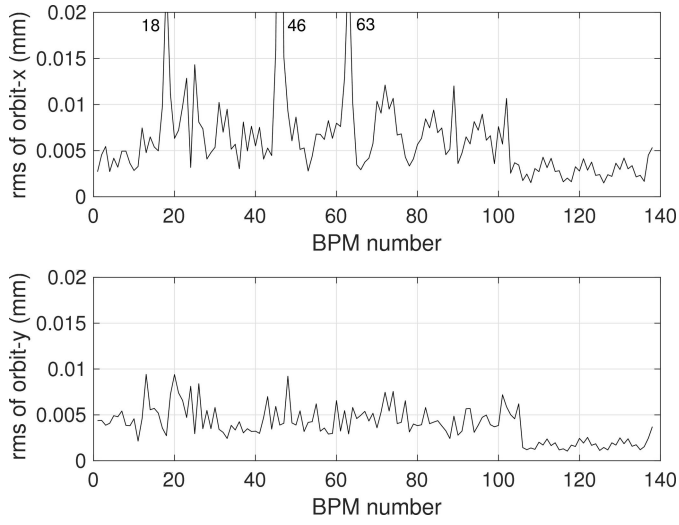

Figure 8
Orbit r.m.s. of 1000 shots of orbit for the horizontal (top) and vertical (bottom) planes, from the injector to the main dump. The beam repetition rate is 30 Hz. The BPMs at the dispersive points (BC1, BC2 and BC3H) are 18, 46, and 63, respectively. The HX undulator line (HX1) is from a BPM number of 112 to 133.

4.5. Laser heater impact on FEL performance

MBI was expected to be more pronounced in the 3-BC scheme than in the 2-BC schemes. However, the actual 3-BC scheme operation revealed that this is not as serious an issue as expected, and in some cases MBI is too weak to deteriorate the FEL performance. The laser heater implemented at the PAL-XFEL successfully suppresses microbunching instability. Fig. 9 shows the 9.7 keV FEL intensity as a function of the laser heater IR laser energy. One can see that the laser heater system helps to suppress the microbunching instability to increase the FEL intensity, whereas a further

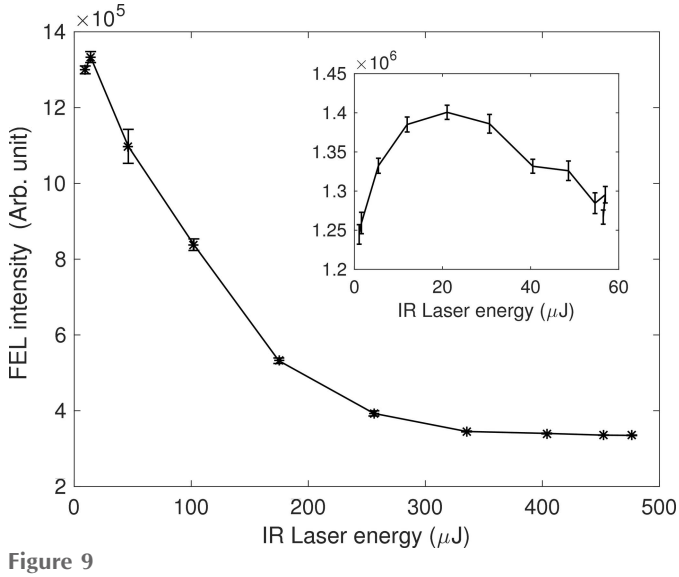

Figure 9
9.7 keV FEL intensity as a function of the laser heater IR laser energy. The inset shows a finer measurement around the peak of the FEL intensity.

increase in IR laser energy reduces the FEL intensity because of the corresponding increase in slice energy spread.

5. FEL performance achieved by the 3-BC scheme operation

5.1. FEL intensity

Fig. 10 shows the available FEL intensity per pulse as a function of photon energy, which has been gradually improved since the FEL user service operation began in June 2017 and is now routinely deliverable to beamlines. The mJ-level intensity was achieved for photon energies from 2.8 keV to 14.4 keV, and it is below 0.5 mJ from 2.0 keV to 2.5 keV. The improvement of FEL intensity is still going on towards the 2 mJ level as at the photon energy of around 9 keV. To deliver a different wavelength FEL, we are changing the e-beam energy from 10.4 GeV for 14.4 keV to 3.88 GeV for 2 keV FEL instead of changing the undulator gap (Yang *et al.*, 2018). The undulator parameter, K (Huang & Kim, 2007), is kept at 1.87, which is highest at the practically reachable undulator gap distance of 9.0 mm, to maximize the FEL gain for those photon energies.

We have improved the FEL intensity remarkably through the Twiss parameter matching at the X-linearizer, L4 and the undulator line, optimizing the transverse position of the electron beam at the X-band linearizer to minimize a transverse RF kick along the bunch, and a proper undulator tapering (Yang *et al.*, 2018). The FEL beam pulse duration measured by the cross-correlation method is 24.7 ± 0.7 fs at FWHM (Ding *et al.*, 2012), and the measured e-beam length is 6.18 ± 0.46 µm (48 fs at FWHM), which means that roughly 51% of the electron beam pulse in length contributes to FEL lasing. The portion of lasing in the e-beam bunch has increased as the FEL intensity was increased by minimizing the tilt along the bunch in the transverse planes. A relatively low FEL intensity at the photon energy of 2–2.5 keV is due to a lower e-beam energy.

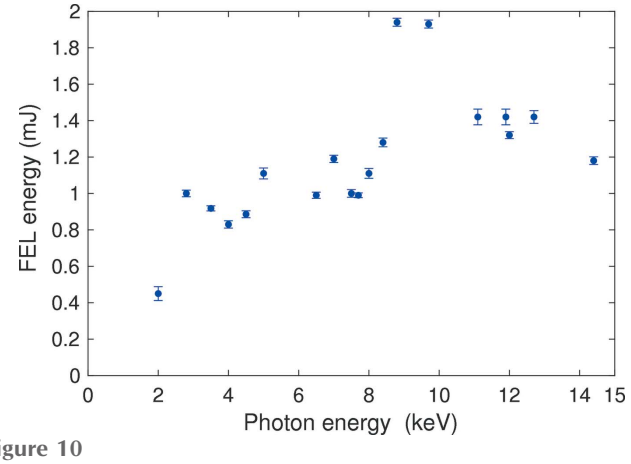

Figure 10
FEL intensity per pulse as a function of photon energy depicted with error bars representing the r.m.s. statistical uncertainties in the measured values. The FEL intensity was measured by using the electron energy loss scan.

The highest FEL intensity at 9.7 keV we achieved is 1.94 ± 0.03 mJ, which corresponds to 1.2×10^{12} photons pulse^{-1}. The FEL intensity was measured by performing an electron energy loss scan, which measures the electron energy loss across undulators by observing the changes in the electron beam position of beam position monitors (BPMs) located at the two different dispersive sections: upstream of the undulator line and the main dump (Loos, 2011). A horizontal plane corrector upstream of the undulator line is used to change the orbit along the undulator line while, at the same time, measuring both the incoming e-beam energy at the undulator upstream BPM and the e-beam energy at the beam dump.

Fig. 11 shows the 9.7 keV FEL beam intensity measured with a quadrant beam position monitor (QBPM) at the beamline for 3.3 min (*a*), demonstrating the short-term stability performance, and for 10 h (*b*), demonstrating the long-term stability. The QBPM sum value was calibrated by the electron energy loss scan to be translated to the FEL intensity. The measured intensity fluctuation is as small as 3.1% in r.m.s., calculated from the short-term data. The long-term stability performance of the FEL intensity is also quite impressive, with a 10 h amplitude jitter of 4.3% in r.m.s., and a drop of FEL intensity caused by e-beam loss did not occur at all during the 10 h operation time. Fig. 11(*b*) reveals that all accelerator systems exhibit a high reliability of performance,

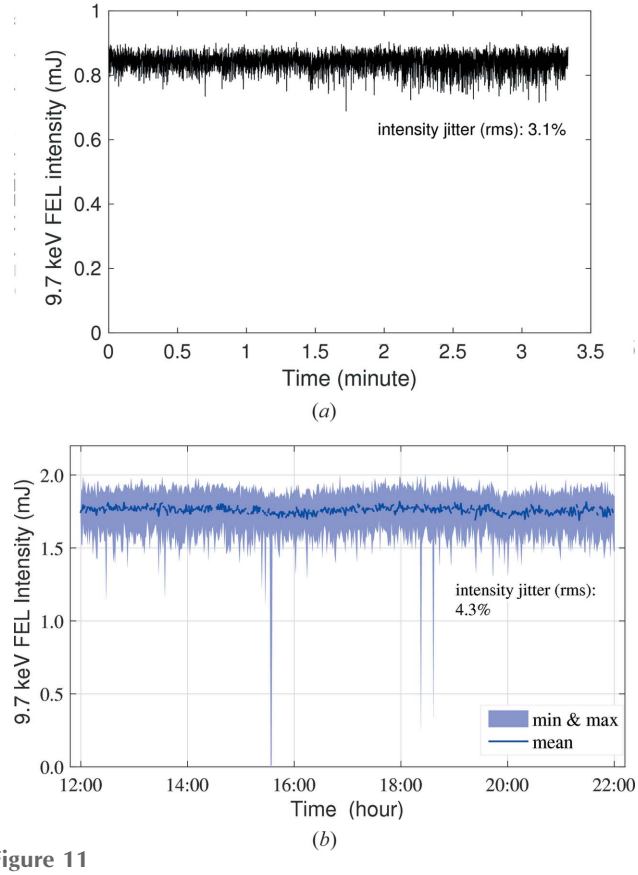

Figure 11
9.7 keV FEL beam intensity measured for 3.3 min (*a*) and 10 h (*b*) during the user service operation using QBPM at the beamline. In (*a*) and (*b*) the QBPM data are converted to FEL intensity calibrated with the electron energy loss scan.

particularly the klystron modulators, which utilize state-of-the art technology (Kim *et al.*, 2015).

The fluctuations of the radiation pulse energy at the end of the exponential gain regime are equal to $1/\sqrt{M}$, where M is the number of longitudinal modes. The coherence length in the exponential gain regime, $l_c = \lambda_r/2\sqrt{\pi}\rho$, where ρ is the FEL parameter (Huang & Kim, 2007) and λ_r is the radiation wavelength, is calculated to be 0.22 fs for 9.7 keV. The FEL beam pulse duration measured by using the cross-correlation method (Ding *et al.*, 2012) is 24.7 $\pm$ 0.7 fs at FWHM, $M \simeq 24.7/0.22 = 112$, and the FEL fluctuation at the end of the exponential gain regime is calculated to be 9.5%. Fluctuations in the radiation pulse energy at the saturation point decrease by a factor of approximately three with respect to the end of the exponential gain regime (Schneidmiller & Yurkov, 2016, 2018), which corresponds to 3.2% for the 9.7 keV FEL, very close to the measurement (3.1%).

5.2. FEL central wavelength jitter

Fig. 12 shows the central wavelength jitter of the 14.4 keV SASE FEL. The measured central wavelength jitter is as small as 3.4 eV in r.m.s. as shown in Fig. 12(*b*), five times smaller than the SASE bandwidth at FWHM (15.5 eV), and corresponds to a relative central wavelength jitter of 2.4×10^{-4} (= 3.4 eV/14.4 keV). The SASE bandwidth is calculated from the average of 1000 shots [average spectrum in Fig. 12(*a*)]. The measured central wavelength jitter of the 6.99 keV FEL is as small as 2.0 eV in r.m.s., which corresponds to a relative central wavelength jitter of 2.9×10^{-4} (= 2 eV/6.99 keV). These small wavelength jitters are attributed to the small e-beam energy jitter of 1.3×10^{-4} (see Section 4.2). The SASE FEL wavelength jitters (2.9×10^{-4} for 6.99 keV and 2.4×10^{-4} for 14.4 keV) are approximately two times the relative e-beam energy jitter (0.013%).

5.3. FEL pointing jitter

Fig. 13 shows the transverse position jitter of the 9.7 keV FEL beam measured for half an hour using the YAG screen monitor located 29 m downstream from the last undulator (see Fig. 1). The FEL beam sizes measured with the YAG screen are 119.1 µm (horizontal) and 133.3 µm in r.m.s. (vertical). The measured position jitter is 10.4 µm in r.m.s. in the horizontal plane and 10.9 µm in the vertical plane, which correspond to 8.7% and 8.2% of the beam size of the horizontal and vertical planes, respectively. It can be translated to the FEL beam divergence angle and its pointing jitter as 1.7 µrad and 0.15 µrad in r.m.s., respectively, which is based on the distance of 70 m from the FEL beam source point to the YAG screen.

6. Conclusions

Start-to-end simulations for the effects of RF jitter on the electron beam performance show that the 3-BC scheme compared with the 2-BC is less subject to RF jitters, which are the most dominant error sources in actual operation. Using the 3-BC scheme enables the delivery of a very stable electron

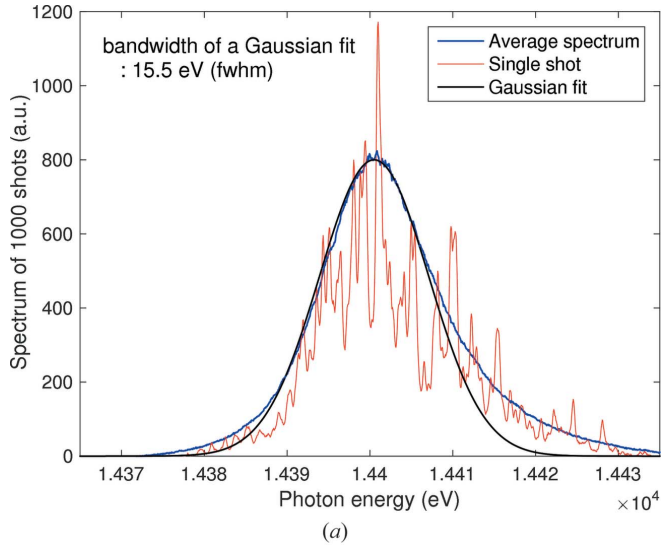

Figure 12
(*a*) Single-shot spectrum of the 14.4 keV SASE FEL measured using a single-shot spectrometer with Si-111 crystal. It is overlaid with the average of 1000 shots and a Gaussian fit. (*b*) Histogram of central wavelengths of 1000 shots of single-shot spectrum.

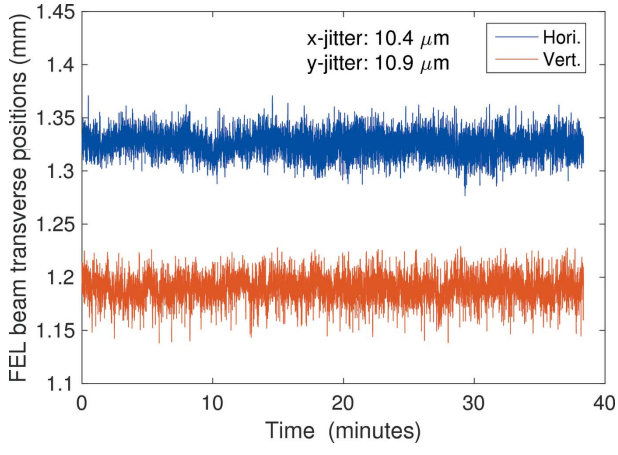

Figure 13
Transverse positions of the 9.7 keV FEL beam measured for half an hour using the YAG screen monitor located 29 m downstream from the last undulator.

beam, in terms of emittance, energy stability, arrival timing and orbit stability, to the undulator line, which subsequently generates a very stable FEL beam. Although initially thought to be a potential concern in the 3-BC scheme, actual operation revealed that microbunching instability is not as serious an issue as expected, and in some cases the MBI is too weak to deteriorate the FEL performance.

The measurement of the e-beam transverse profile along the undulator line using wire scanners made it possible to accurately measure the projected emittance and Twiss parameters, and apply a matching of the measured Twiss parameter to the design lattice. Using this emittance measurement and lattice matching, we could maintain the projected emittance below 0.72 mm mrad (horizontal) and 0.58 mm mrad (vertical) from the injector to the undulator line.

Together with the high performance of the linac RF system, the 3-BC scheme allows reliable operation of PAL-XFEL with unprecedented stability in terms of arrival timing, pointing and intensity. A timing jitter of smaller than 15 fs, a transverse position jitter of smaller than 10% of the photon beam size, and an FEL intensity jitter of smaller than 5% are consistently achieved. The measured central wavelength jitter is as small as 2.4×10^{-4}, two times smaller than the FEL parameter of 5.0×10^{-4}, which is attributed to the small e-beam energy jitter of 0.013%.

Still, there should be things to improve for much better performance; for example, the X-band RF system stability needs to be improved further, and there should be better parameter settings with respect to acceleration and bunching for the 3-BC scheme.

Acknowledgements

The authors would like to thank Henrik Loos for his appreciable help in use of the MATLAB control programs.

Funding information

This research was supported by the Ministry of Science and ICT of Korea and partly by the Basic Science Research Program (Grant No. 2017R1A2B4007274) through the National Research Foundation of Korea (NRF) funded by the Ministry of Science and ICT of Korea.

References

Borland, M. (2000). *Elegant: A Flexible SDDS-Compliant Code for Accelerator Simulation.* ANL APS Report No. LS-287. Argonne National Laboratory, Illinois, USA.
Borland, M. (2001*a*). *Phys. Rev. ST Accel. Beams*, **4**, 074201.
Borland, M. (2001*b*). *Phys. Rev. ST Accel. Beams*, **4**, 070701.
Chae, M. S., Hong, J. H., Parc, Y. W., Ko, I. S., Park, S. J., Qian, H. J., Huang, W. H. & Tang, C. X. (2011). *Phys. Rev. ST Accel. Beam*, **14**, 104203.
Di Mitri, S., Cornacchia, M. & Spampinati, S. (2013). *Phys. Rev. Lett.* **110**, 014801.
Ding, Y., Bane, K. L. F., Colocho, W., Decker, F.-J., Emma, P., Frisch, J., Guetg, M. W., Huang, Z., Iverson, R., Krzywinski, J., Loos, H., Lutman, A., Maxwell, T. J., Nuhn, H.-D., Ratner, D., Turner, J., Welch, J. & Zhou, F. (2016). *Phys. Rev. ST Accel. Beams*, **19**, 100703.
Ding, Y., Decker, F. J., Emma, P., Feng, C., Field, C., Frisch, J., Huang, Z., Krzywinski, J., Loos, H., Welch, J., Wu, J. & Zhou, F. (2012). *Phys. Rev. Lett.* **109**, 254802.
Douglas, D. (1998). Thomas Jefferson National Accelerator Facility Report No. JLAB-TN-98–012. Thomas Jefferson National Accelerator Facility, Newport News, Virginia, USA.
Emma, P., Akre, R., Arthur, J., Bionta, R., Bostedt, C., Bozek, J., Brachmann, A., Bucksbaum, P., Coffee, R., Decker, F.-J., Ding, Y., Dowell, D., Edstrom, S., Fisher, A., Frisch, J., Gilevich, S., Hastings, J., Hays, G., Hering, P., Huang, Z., Iverson, R., Loos, H., Messerschmidt, M., Miahnahri, A., Moeller, S., Nuhn, H.-D., Pile, G., Ratner, D., Rzepiela, J., Schultz, D., Smith, T., Stefan, P., Tompkins, H., Turner, J., Welch, J., White, W., Wu, J., Yocky, G. & Galayda, J. (2010). *Nat. Photon.* **4**, 641–647.
Hajima, R. (2003). *Jpn. J. Appl. Phys.* **42**, L974–L976.
Heifets, S., Stupakov, G. & Krinsky, S. (2002). *Phys. Rev. ST Accel. Beams*, **5**, 064401.
Huang, Z. & Kim, K.-J. (2002). *Phys. Rev. ST Accel. Beams*, **5**, 074401.
Huang, Z. & Kim, K.-J. (2007). *Phys. Rev. ST AB* **10**, 034801.
Ishikawa, T. *et al.* (2012). *Nat. Photon.* **6**, 540–544.
Kang, H.-S., Han, J. H., Kang, T.-H. & Ko, I. S. (2012*a*). *Proceedings of the 34th International Free-Electron Laser Conference (FEL2012)*, 26–31 August 2012, Nara, Japan, pp. 309–312. TUPD34.
Kang, H.-S., Ko, I. S., Nam, S. H., Cho, M.-H. & Yi, C. H. (2011). *Proceedings of the 33rd International Free Electron Laser Conference (FEL2011)*, 22–26 August 2011, Shanghai, China, pp. 447–450. THOA4.
Kang, H., Min, C., Heo, H., Kim, C., Yang, H., Kim, G., Nam, I., Baek, S. Y., Choi, H., Mun, G., Park, B. R., Suh, Y. J., Shin, D. C., Hu, J., Hong, J., Jung, S., Kim, S., Kim, K., Na, D., Park, S. S., Park, Y. J., Han, J., Jung, Y. G., Jeong, S. H., Lee, H. G., Lee, S., Lee, S., Lee, W., Oh, B., Suh, H. S., Parc, Y. W., Park, S., Kim, M. H., Jung, N., Kim, Y., Lee, M., Lee, B., Sung, C., Mok, I., Yang, J., Lee, C., Shin, H., Kim, J. H., Kim, Y., Lee, J. H., Park, S., Kim, J., Park, J., Eom, I., Rah, S., Kim, S., Nam, K. H., Park, J., Park, J., Kim, S., Kwon, S., Park, S. H., Kim, K. S., Hyun, H., Kim, S. N., Kim, S., Hwang, S., Kim, M. J., Lim, C., Yu, C., Kim, B., Kang, T., Kim, K., Kim, S., Lee, H., Lee, H., Park, K., Koo, T., Kim, D. & Ko, I. S. (2017). *Nat. Photon.* **11**, 708–713.
Kang, H.-S. *et al.* (2014). *PAL-XFEL Technical Design Report.* Pohang Accelerator Laboratory, Pohang, South Korea.
Kang, H.-S. *et al.* (2019). In preparation.
Kim, C., Baek, S. Y., Choi, H. J., Hong, J. H., Kang, H.-S., Kim, G., Kim, J. H., Ko, I. S., Lee, S. J., Mun, G., Oh, B. G., Park, B. R., Shin, D. C., Suh, Y. J. & Yang, H. (2016). *Proceedings of the 5th International Beam Instrumentation Conference (IBIC2016)*, 11–15 September 2016, Barcelona, Spain, pp. 11–13. MOBL01.
Kim, G., Kang, H.-S., Kim, C., Oh, B. G. & Shin D. C. (2018). *Proceedings of the 7th International Beam Instrumentation Conference (IBIC2018)*, 9–13 September 2018, Shanghai, China, pp. 445–447. WEPB09.
Kim, S. H., Kang, H.-S., Kim, G. H., Ko, I. S., Kwon, S. J., Lee, H.-S., Park, S. S., Park, Y. J., Cho, M.-H., Jang, K. Y. Shin, H. S., Kim, D. S., Lee, S. Y. & Seo M. (2015). *Proceedings of the 37th International Free Electron Laser Conference (FEL2015)*, 23–28 August 2015, Daejeon, Korea pp. 89–92. MOP029.
Lee, J., Han, J., Lee, S., Hong, J., Kim, C. H., Min, C. K. & Ko, I. S. (2017). *Nucl. Instrum. Methods Phys. Res. A*, **843**, 39–45.
Loos, H. (2011). *Proceedings of the 33rd International Free Electron Laser Conference (FEL2011)*, 22–26 August 2011, Shanghai, China, pp. 166–172. TUOBI3.
Milne, C., Schietinger, T., Aiba, M., Alarcon, A., Alex, J., Anghel, A., Arsov, V., Beard, C., Beaud, P., Bettoni, S., Bopp, M., Brands, H., Brönnimann, M., Brunnenkant, I., Calvi, M., Citterio, A.,

Craievich, P., Csatari Divall, M., Dällenbach, M., D'Amico, M., Dax, A., Deng, Y., Dietrich, A., Dinapoli, R., Divall, E., Dordevic, S., Ebner, S., Erny, C., Fitze, H., Flechsig, U., Follath, R., Frei, F., Gärtner, F., Ganter, R., Garvey, T., Geng, Z., Gorgisyan, I., Gough, C., Hauff, A., Hauri, C., Hiller, N., Humar, T., Hunziker, S., Ingold, G., Ischebeck, R., Janousch, M., Juranić, P., Jurcevic, M., Kaiser, M., Kalantari, B., Kalt, R., Keil, B., Kittel, C., Knopp, G., Koprek, W., Lemke, H., Lippuner, T., Llorente Sancho, D., Löhl, F., Lopez-Cuenca, C., Märki, F., Marcellini, F., Marinkovic, G., Martiel, I., Menzel, R., Mozzanica, A., Nass, K., Orlandi, G., Ozkan Loch, C., Panepucci, E., Paraliev, M., Patterson, B., Pedrini, B., Pedrozzi, M., Pollet, P., Pradervand, C., Prat, E., Radi, P., Raguin, J., Redford, S., Rehanek, J., Réhault, J., Reiche, S., Ringele, M., Rittmann, J., Rivkin, L., Romann, A., Ruat, M., Ruder, C., Sala, L., Schebacher, L., Schilcher, T., Schlott, V., Schmidt, T., Schmitt, B., Shi, X., Stadler, M., Stingelin, L., Sturzenegger, W., Szlachetko, J., Thattil, D., Treyer, D., Trisorio, A., Tron, W., Vetter, S., Vicario, C., Voulot, D., Wang, M., Zamofing, T., Zellweger, C., Zennaro, R., Zimoch, E., Abela, R., Patthey, L. & Braun, H. (2017). *Appl. Sci.* **7**, 720.

Pflueger, J., Bagha-Shanjani, M., Berndgen, K., Beckmann, A., Biermordt, P., Deron, G., Englisch, U., Karabekyan, S., Ketenoglu, B., Knoll, M., Li, Y., Wolff-Fabris, F. & Yakopov, M. (2013). *Proceedings of the 35th International Free-Electron Laser Conference (FEL2013)*, New York, NY, USA, 26–30 August 2013, pp. 367–371. TUPSO60.

Saldin, E. L., Schneidmiller, E. A. & Yurkov, M. V. (2002). *Nucl. Instrum. Methods Phys. Res. A*, **490**, 1–8.

Saldin, E. L., Schneidmiller, E. A. & Yurkov, M. V. (2004). *Nucl. Instrum. Methods Phys. Res. A*, **528**, 355–359.

Schneidmiller, E. A. & Yurkov, M. V. (2016). *Proceedings of the 7th International Particle Accelerator Conference (IPAC2016)*, 8–13 May 2016, Busan, Korea, pp. 738–740. MOPOW013.

Schneidmiller, E. A. & Yurkov, M. V. (2018). *CERN Yellow Reports: School Proceedings*, Vol. 1, pp. 539–596. http://dx.doi.org/10.23730/CYRSP-2018-001.539.

Shin, D. C., Hong, J. H., Kang, H.-S., Kim, C., Kim, G. & Min, C.-K. (2018). *Proceedings of the 7th International Beam Instrumentation Conference (IBIC2018)*, 9–13 September 2018, Shanghai, China, pp. 400–403. WEPA15.

Venturini, M., Papadopoulos, C. F., Qiang J., Ding, Y., Emma, P., Huang, Z., Marcus, G., Marinelli, A., Nosochkov, Y., Raubenheimer, T. O., Wang, L. & Woodley M. (2015). *Proceedings of the 6th International Particle Accelerator Conference (IPAC'15)*, 3–8 May 2015, Richmond, VA, USA, pp. 1843–1845. TUPMA003.

Weise, H. & Decking, W. (2017). *Proceedings of the 38th International Free-Electron Laser Conference (FEL2017)*, 20–25 August 2017, Santa Fe, NM, USA, pp. 9–13. MOC03.

Yang, H., Kim, G. & Kang, H.-S. (2018). *Nucl. Instrum. Methods Phys. Res. A*, **911**, 51–54.

Zhou, F. *et al.* (2015). *Phys. Rev. ST Accel. Beams* **18**, 050702.